HHS Public Access

Author manuscript

Mol Imaging Biol. Author manuscript; available in PMC 2018 December 01.

Published in final edited form as:

Mol Imaging Biol. 2017 December ; 19(6): 867–877. doi:10.1007/s11307-017-1082-x.

Fluorine-18 Labeling of the HER2-Targeting Single-Domain Antibody 2Rs15d Using a Residualizing Label and Preclinical Evaluation

Zhengyuan Zhou[1], **Ganesan Vaidyanathan**[1], **Darryl McDougald**[1], **Choong Mo Kang**[1], **Irina Balyasnikova**[2], **Nick Devoogdt**[3], **Angeline N. Ta**[4], **Brian R. McNaughton**[4], and **Michael R. Zalutsky**[1]

[1]Department of Radiology, Duke University Medical Center, Box 3808, Durham, NC, USA

[2]The Feinberg School of Medicine, Northwestern University, Chicago, IL, 60611, USA

[3]In Vivo Cellular and Molecular Imaging Laboratory, Vrije Universiteit Brussel, 1090, Brussels, Belgium

[4]Department of Chemistry, Colorado State University, Fort Collins, CO, 80523, USA

Abstract

Purpose—Our previous studies with F-18-labeled anti-HER2 single-domain antibodies (sdAbs) utilized 5F7, which binds to the same epitope on HER2 as trastuzumab, complicating its use for positron emission tomography (PET) imaging of patients undergoing trastuzumab therapy. On the other hand, sdAb 2Rs15d binds to a different epitope on HER2 and thus might be a preferable vector for imaging in these patients. The aim of this study was to evaluate the tumor targeting of F-18 -labeled 2Rs15d in HER2-expressing breast carcinoma cells and xenografts.

Procedures—sdAb 2Rs15d was labeled with the residualizing labels *N*-succinimidyl 3-((4-(4-[^{18}F]fluorobutyl)-1*H*-1,2,3-triazol-1-yl)methyl)-5-(guanidinomethyl)benzoate ([^{18}F]RL-I) and *N*-succinimidyl 4-guanidinomethyl-3-[^{125}I]iodobenzoate ([^{125}I]SGMIB), and the purity and HER2-specific binding affinity and immunoreactivity were assessed after labeling. The biodistribution of I-125- and F-18-labeled 2Rs15d was determined in SCID mice bearing subcutaneous BT474M1 xenografts. MicroPET/x-ray computed tomograph (CT) imaging of [^{18}F]RL-I-2Rs15d was performed in this model and compared to that of nonspecific sdAb [^{18}F]RL-I-R3B23. MicroPET/CT imaging was also done in an intracranial HER2-positive breast cancer brain metastasis model after administration of 2Rs15d-, 5F7-, and R3B23-[^{18}F]RL-I conjugates.

Results—[^{18}F]RL-I was conjugated to 2Rs15d in 40.8 ± 9.1 % yield and with a radiochemical purity of 97–100 %. Its immunoreactive fraction (IRF) and affinity for HER2-specific binding were 79.2 ± 5.4 % and 7.1 ± 0.4 nM, respectively. [^{125}I]SGMIB was conjugated to 2Rs15d in 58.4 ± 8.2 % yield and with a radiochemical purity of 95–99 %; its IRF and affinity for HER2-specific binding were 79.0 ± 12.9 % and 4.5 ± 0.8 nM, respectively. Internalized radioactivity in BT474M1

Correspondence to: Ganesan Vaidyanathan; ganesan.v@duke.edu.

Compliance with Ethical Standards

Conflict of Interest

The authors declare that they have no conflict of interest.

cells *in vitro* for [^{18}F]RL-I-2Rs15d was 43.7 ± 3.6, 36.5 ± 2.6, and 21.7 ± 1.2 % of initially bound radioactivity at 1, 2, and 4 h, respectively, and was similar to that seen for [^{125}I]SGMIB-2Rs15d. Uptake of [^{18}F]RL-I-2Rs15d in subcutaneous xenografts was 16–20 %ID/g over 1–3 h. Subcutaneous tumor could be clearly delineated by microPET/CT imaging with [^{18}F]RL-I-2Rs15d but not with [^{18}F]RL-I-R3B23. Intracranial breast cancer brain metastases could be visualized after intravenous administration of both [^{18}F]RL-I-2Rs15d and [^{18}F]RL-I-5F7.

Conclusions—Although radiolabeled 2Rs15d conjugates exhibited lower tumor cell retention both *in vitro* and *in vivo* than that observed previously for 5F7, given that it binds to a different epitope on HER2 from those targeted by the clinically utilized HER2-targeted therapeutic antibodies trastuzumab and pertuzumab, F-18-labeled 2Rs15d has potential for assessing HER2 status by PET imaging after trastuzumab and/or pertuzumab therapy.

Keywords

Single-domain antibody; Trastuzumab; HER2; Fluorine-18; PET; Breast cancer

Introduction

Up to about 25 % of breast cancers express human epidermal growth factor receptor 2 (HER2), and overexpression of HER2 is associated with tumor aggressiveness and poor prognosis [1, 2]. This has led to the development of a variety of HER2-targeted therapies including the anti-HER2 antibodies trastuzumab and pertuzumab, T-DM1 (Kadcyla®)—an antibody-drug conjugate derived from trastuzumab and emtansine (DM1), and the tyrosine kinase inhibitor lapatinib [3–5]. Because only a subset of breast cancer patients has HER2-expressing tumors, reliable evaluation of HER2 status is a critical step in selecting patients who might benefit from these HER2-specific treatments. Current methods for the determination of HER2 status, immunohistochemistry, and fluorescence *in situ* hybridization are invasive, requiring biopsy samples [6]. Furthermore, these techniques are of limited use for dealing with the heterogeneous nature of HER2 expression in the primary tumor and the significant discordance in HER2 expression in primary tumor and metastases as well as among metastases in an individual patient [7, 8]. In contrast, molecular imaging techniques such as positron emission tomography (PET) are noninvasive and can provide global status of HER2 in real time [9]. Moreover, determination of HER2 status by PET imaging can also be used to evaluate response to HER2-targeted therapies.

A number of targeting vectors including intact antibodies, F(ab′)$_2$ fragments, minibodies, diabodies, and affibodies have been labeled with various positron emitters and evaluated for the determination of HER2 status by PET [10–14]. Camelid-derived single-domain antibodies (sdAb), a.k.a. VHH molecules or nanobodies, are attractive for this purpose because of their ease of production, excellent stability, high water solubility, low immunogenicity, and nanomolar to picomolar affinity [15, 16]. Their molecular weight (12–15 kDa), a tenth of intact antibodies, facilitates deeper tumor penetration compared with intact antibodies. A significant advantage for PET imaging applications is that their fast blood clearance makes them compatible for use with clinically amenable short-lived positron emitters F-18 and Ga-68 [17, 18].

In a previous study, we evaluated the possibility of labeling a HER2-specific sdAb with F-18 and developed a novel residualizing F-18 labeling method, to maximize trapping of radioactivity in tumor cells after receptor internalization [19]. Although excellent tumor targeting properties were observed for F-18-labeled 5F7 anti-HER2 conjugate, this sdAb binds to the C-terminus of domain IV of HER2 [20], and its HER2 binding can be blocked by trastuzumab [21]. Unfortunately, this compromises its potential utility in radiolabeled form as a PET agent for evaluating response to trastuzumab therapy as it will not be able to differentiate, for example, between low tumor uptake due to HER2 blocking by circulating trastuzumab and receptor downregulation [22]. An intriguing approach that circumvents this problem would be to utilize 2Rs15d, identified from a panel of anti-HER2 sdAbs [23] as a molecule with good affinity and tumor targeting but recognizing a different epitope on HER2 from those targeted by the clinically relevant therapeutic antibodies trastuzumab and pertuzumab [18, 24].

The goal of the current study was to label 2Rs15d using the residualizing label *N*-succinimidyl 3-((4-(4-[^{18}F]fluorobutyl)-1*H*-1,2,3-triazol-1-yl)methyl)-5-(guanidinomethyl)benzoate ([^{18}F]RL-I or [^{18}F]SFBTMGMB; Fig. 1) [19, 25] and evaluate the potential utility of this radioconjugate for imaging HER2-expressing tumors by PET. Studies were performed in BT474M1 breast carcinoma cells as well as in subcutaneous and intracranial xenografts derived from this line and included comparisons to 2Rs15d radioiodinated with the prototypical residualizing prosthetic agent SGMIB [26].

Materials and Methods

General

All reagents were purchased from Sigma-Aldrich except where noted. Sodium [^{125}I]iodide (81.4 TBq/mmol) in 0.1 N NaOH was obtained from PerkinElmer Life and Analytical Sciences (Boston, MA). *N*-succinimidyl 4-guanidinomethyl-3-[^{125}I]iodobenzoate ([^{125}I]SGMIB) [26] and the F-18 residualizing prosthetic agent [^{18}F]RL-I [25] were synthesized as reported previously. High-pressure liquid chromatography (HPLC) was performed using a Beckman Gold HPLC system equipped with a Model 126 programmable solvent module, a Model 168 diode array detector, and Beckman System Gold remote interface module SS420X; data were acquired using 32 Karat® software. Radioactivity was detected using an IN/US γ-RAM detector and Laura Lite® software (IN/US Systems, Tampa, FL; now LabLogic); this system has the capability to detect two radionuclides simultaneously. Disposable PD 10 desalting columns for gel filtration were purchased from GE Healthcare (Piscataway, NJ). Instant thin-layer chromatography (ITLC) was performed using silica gel-impregnated glass fiber sheets (Pall Corporation, East Hills, NY) with PBS, pH 7.4, as the mobile phase. Developed sheets were analyzed for radioactivity either using the TLC scanner described above or by cutting the sheet into small strips and counting them in an LKB 1282 (Wallac, Finland) automated gamma counter. Radioactivity levels in various samples were assessed using this LKB 1282 device or using a PerkinElmer Wizard II (Shelton, CT) automated gamma counter.

Single-Domain Antibodies, Cells, and Culture Conditions

Single-domain antibody 5F7 was produced and purified as described [27, 28]. Details of the production, purification, and characterization of 2Rs15d sdAb have been reported previously [23, 24]. An anti-paraprotein sdAb R3B23 [29], with no binding to HER2, was used as a control to determine nonspecific uptake. The sdAbs used in these experiments were devoid of any tags such as His-tag or Cys-tag. Cell culture reagents were purchased from Invitrogen (Grand Island, NY). BT474M1 human breast carcinoma cells [30], a more tumorigenic version of the parental BT474 cell line, were grown in DMEM/F12 medium containing 10 % fetal calf serum (FCS), streptomycin (100 μg/ml), and penicillin (100 IU/ml) (Sigma-Aldrich, MO). The cells were cultured at 37 °C in a 5 % CO_2 humidified incubator.

Radiolabeling of Single-Domain Antibodies

The methods for radiolabeling sdAb 2Rs15d with [^{125}I]SGMIB and [^{18}F]RL-I were essentially identical to those reported previously for labeling 5F7 with these prosthetic agents [25, 31]. Briefly, a solution of 2Rs15d in borate buffer, pH 8.5 (100 μg in 50 μl), was added to the dried prosthetic agent (0.37–0.56 GBq for [^{18}F]RL-I and 0.04–0.11 GBq for [^{125}I]SGMIB), and the mixture was incubated at 20 °C for 20 min. Labeled protein was isolated by gel filtration over a PD10 column preconditioned with human serum albumin (HSA) to minimize nonspecific binding and eluted with PBS. R3B23 was labeled using [^{18}F]RL-I in a similar fashion. The purity of labeled sdAbs was determined by trichloroacetic acid (TCA) precipitation, ITLC, and SDS-PAGE/phosphor imaging as described previously [25, 27, 31]. In some cases, size-exclusion HPLC was also performed. For this, a TSKgel Super SW2000 4.6 mm × 30 cm column attached with a 4.6 mm × 3.5 cm guard column (Tosoh Bioscience, Montgomeryville, PA) was equilibrated and eluted with PBS, pH 7.0, at a flow rate of 0.3 ml/min with a run time of 25 min. Under these conditions, all sdAbs eluted with a retention time of 16 min.

Immunoreactivity and K_D Determination of Radiolabeled 2Rs15d

The immunoreactive fraction of radiolabeled sdAb conjugates was determined by the Lindmo method [32] using magnetic beads coated with the extracellular domain of HER2 or, as a negative control, with HSA, prepared as described [25, 27, 31]. Briefly, aliquots of labeled sdAb (~5 ng) were incubated in duplicate with three doubling concentrations of both positive (HER2) and negative (HSA) beads. Reciprocals of the percentage of specific binding (positive minus negative) were plotted against the reciprocals of bead concentration, and from this, the immunoreactive fraction was calculated, indicating specific binding at the infinite antigen concentration [32].

For the saturation binding assay to determine radiolabeled sdAb HER2 binding affinity, BT474M1 cells were plated in 24-well plates at a density of 8×10^4 cells/well/ml and incubated overnight at 37 °C. Subsequently, the cells were allowed to acclimatize at 4 °C for 30 min prior to the addition of increasing concentrations of radiolabeled 2Rs15d (0.1–300 nM; 0.6 ml total volume per well). The cells were incubated with the tracer at 4 °C for 2 h, the medium containing unbound radioactivity was removed, and the cells were washed twice with cold PBS. Finally, the cells were solubilized by treatment with 0.5 ml 0.1 % SDS at 37 °C for 10 min. Cell-associated radioactivity was counted using an automated gamma

counter. To determine nonspecific binding, parallel assays were performed by co-incubating cells with a 100-fold excess of 2Rs15d. The data were fit using GraphPad Prism software to determine the K_D value.

In Vitro Internalization Assays

These assays were performed in a paired label format as described for other radiolabeled sdAbs [19, 31]. BT474M1 cells at a density of 8×10^5 cells per well in 3 ml medium were plated in six-well plates. After overnight incubation at 37 °C, the cells were brought to 4 °C and incubated for 30 min. The medium was removed and replenished with 2 ml fresh medium containing F-18- and I-125 labeled sdAbs (5 nM each), and the cells were further incubated at 4 °C for 1 h. Cell culture supernatants containing unbound radioactivity were removed, and 2 ml fresh medium at 37 °C was added. The cells were brought to 37 °C and incubated for 1, 2, and 4 h and processed as follows. Cell culture supernatants were collected, and the cells were washed with an acidic buffer consisting of 50 mM glycine-HCl/0.1 M NaCl, pH 2.8, to strip off the surface-bound radioactivity. Finally, the cells were lysed by incubating with 0.1 % SDS (1 ml). Radioactivity in cell lysates, acid washes, and cell culture supernatants was counted, and from these values, the percentage of radioactivity initially bound to the cells that were present in cell culture supernatants, acid washes, and cell lysates was calculated. To determine nonspecific uptake, a parallel experiment was performed as above but with a 100-fold molar excess of 2Rs15d added along with the labeled sdAb preparations.

Biodistribution Studies

All experiments involving animals were performed using a protocol approved by the Duke University Institutional Animal Care and Use Committee. Subcutaneous BT474M1 tumor xenografts in 10–12-week-old NOD.CB17-Prkdcscid/J female mice weighing about 20 g were established as described previously [27]. When tumors reached a volume of 300–500 mm^3, a paired label experiment was performed to directly compare the biodistribution of [^{18}F]RL-I-2Rs15d with that of [^{125}I]SGMIB-2Rs15d. For this, 185 kBq (5 μCi; 0.7 μg) of [^{125}I]SGMIB-2Rs15d and 222 kBq (6 μCi; 0.8 μg) of [^{18}F]RL-I-2Rs15d were injected intravenously into three groups of five mice and serial necropsies were performed at 1, 2, and 3 h post-injection (p.i.). At each time point, blood and urine were collected, and mice were killed by isoflurane overdose. Tumor and solid tissues were isolated, blot-dried, and weighed. Radioactivity in these tissues, as well as in blood and urine, was counted along with injection standards using an automated gamma counter. From these data, the percentage of the injected dose (ID) per organ and per gram of tissue (%ID/g) was calculated. Statistical significance of difference in uptake between co-administered sdAbs was determined by a paired Student's *t* test using the Microsoft Excel program; a *P* value of <0.05 was considered significant.

MicroPET/CT Imaging—Subcutaneous Model

Imaging was performed on a Siemens Inveon microPET/CT system (Malvern, PA) in mice with BT474M1 subcutaneous xenografts. Three mice were imaged at 1, 2, and 3 h after intravenous administration of [^{18}F]RL-I-2Rs15d, one mouse with one batch (5.5 MBq/149 μCi; 13 μg) and the other two with another batch (2.2 MBq/60 μCi; 7.2 μg and 1.7 MBq/46

μCi; 5.4 μg) on a different day. The latter two mice were also imaged at 1 and 2 h after injection of ~3.6 MBq (97 μCi; 8 μg) of [^{18}F]RL-I-R3B23 on the next day. The mice were anesthetized using 2–3 % isoflurane in oxygen and placed prone in the scanner gantry for a 5-min PET acquisition followed by a 5-min CT scan. List-mode PET data were histogram-processed and the images reconstructed using a standard OSEM3D/MAP algorithm—2 OSEM3D iterations and 18 MAP iterations—with a cutoff (Nyquist) of 0.5. Images were corrected for attenuation (based on CT scan) and for radioactive decay. Image analysis was performed using Inveon Research Workplace software. Regions of interest (ROI) were drawn around tumors on the co-registered PET and CT images, and F-18 uptake was expressed as SUV and %ID/g.

MicroPET/CT Imaging—Intracranial Model

MicroPET/CT imaging also was performed in two athymic nu/nu female mice bearing intracranial xenografts of HER2-expressing breast cancer brain metastases, BT474M1BrM3 modified to express firefly luciferase (BT474M1BrM3-Fluc). This model was established as described [33] by implanting ~6 × 10^5 BT474M1BrM3-Fluc cells in the mouse brain and allowing tumors to grow for about 8 weeks prior microPET/CT imaging. Tumor growth was monitored by bioluminescence imaging (data not shown). MicroPET/CT imaging was performed 1 h after tail vein injection of 3.1 MBq (84 μCi; 7 μg) of [^{18}F]RL-I-2Rs15d or 3.3 MBq (90 μCi; 10 μg) of [^{18}F]RL-I-R3B23. One animal was also imaged after administration of ~2.2 MBq (60 μCi; 3 μg) of [^{18}F]RL-I-5F7. The excised brain from one mouse was fixed in 4 % paraformaldehyde and paraffin-embedded. Four-micrometer tissue sections were stained with hematoxylin and eosin (H&E) dye in order to corroborate the imaging and histological findings.

Results

[^{18}F]RL-I-2Rs15d and [^{18}F]RL-I-R3B23 Synthesis

The average yield for labeling 2Rs15d *via* conjugation to [^{18}F]RL-I was 40.8 ± 9.1 % (n = 12) with a specific activity of 0.2–0.8 GBq/mg. The overall radiochemical yield for the synthesis of [^{18}F]RL-I-2Rs15d starting with aqueous [^{18}F]fluo-ride was 3–4 %, and the total duration of the synthesis was 150 min. SDS-PAGE/phosphor imaging analysis of [^{18}F]RL-I-2Rs15d indicated the presence of a single radioactive band with a molecular weight of about 12–13 kDa, corresponding to the molecular weight of a sdAb monomeric species (Fig. 2a). High radiochemical purity of F-18-labeled 2Rs15d was further corroborated by size-exclusion HPLC (Fig. 2b), ITLC (98.2 ± 2.5 %), and TCA precipitability (97.1 ± 0.2 %). The immunoreactive fraction determined by the Lindmo assay for [^{18}F]RL-I-2Rs15d was 79.2 ± 5.4 % (Fig. 2c). A K_D value of 7.1 ± 0.4 nM was obtained from a saturation binding assay using the HER2-expressing BT474M1 cell line (Fig. 2d). The control sdAb R3B23 was labeled with [^{18}F]RL-I in 28.9 ± 7.6 % (n = 2) yield, and SDS-PAGE of the labeled sdAb indicated a purity of >97 %.

[^{125}I]SGMIB-2Rs15d Synthesis

For use in paired label experiments, the [^{125}I]SGMIB-2Rs15d conjugate was produced by reaction of [^{125}I]SGMIB and 2Rs15d with a coupling efficiency of 58.4 ± 8.2 % (n = 7). The

overall radiochemical yield for the synthesis of [^{125}I]SGMIB-2Rs15d starting from [^{125}I]iodide was 25 % in a total duration of 150 min. The radiochemical purity of [^{125}I]SGMIB-2Rs15d, determined by ITLC, SDS-PAGE, TCA precipitation, and size-exclusion HPLC was 95–99 %. The immunoreactive fraction determined by the Lindmo assay for [^{125}I]SGMIB-2Rs15d was 79.0 ± 12.9 %, and the saturation binding assay performed on BT474M1 cells yielded a K_D value of 4.5 ± 0.8 nM.

Paired-Label Internalization of [^{18}F]RL-I-2Rs15d and [^{125}I]SGMIB-2Rs15d

A paired label assay on BT474M1 cells was performed to compare the internalized and total cell-associated radioactivity for 2Rs15d labeled using [^{18}F]RL-I and [^{125}I]SGMIB residualizing labels. As shown in Fig. 3, internalized radioactivity and total cell-associated radioactivity were similar for 2Rs15d labeled using both prosthetic agents and declined with time, particularly in the intracellular radioactivity levels. For example, with [^{18}F]RL-I-2Rs15d, the fraction of activity initially bound to BT474M1 cells declined significantly from 43.7 ± 3.6 % at 1 h to 21.7 ± 1.2 % at 4 h ($P < 0.05$).

Paired-Label Biodistribution of [^{18}F]RL-I-2Rs15d and [^{125}I]SGMIB-2Rs15d in Mice with Subcutaneous BT474M1 Xenografts

The percent of injected dose per gram uptake of I-125 and F-18 in tumor and normal tissues after intravenous co-administration of [^{18}F]RL-I-2Rs15d and [^{125}I]SGMIB-2Rs15d in SCID mice with subcutaneous BT474M1 xenografts are summarized in Table 1. Tumor levels for both tracers were greater than 15 %ID/g and remained stable from 1 to 3 h; however, tumor uptake of [^{18}F]RL-I-2Rs15d was 16–20 % lower ($P < 0.05$) than that of [^{125}I]SGMIB-2Rs15d at all time points. Sequestration of radioactivity from [^{18}F]RL-I-2Rs15d in the liver, spleen, and lungs was five to more than ten times higher than that seen for 2Rs15d radioiodinated using the [^{125}I]SGMIB prosthetic agent. Kidney uptake of [^{18}F]RL-I-2Rs15d was about 15 % higher than that of [^{125}I]SGMIB-2Rs15d. Tumor-to-tissue ratios for [^{18}F]RL-I-2Rs15d in general were much lower than those seen for co-injected [^{125}I]SGMIB-2Rs15d (data for selected tissues shown in Fig. 4). However, except for the kidneys, tumor-to-tissue ratios for [^{18}F]RL-I-2Rs15d were greater than unity for all tissues with values greater than 10:1 observed for the heart, stomach, muscle, blood, bone, and brain by 2 h after injection.

MicroPET/CT Imaging

Maximum intensity projection (MIP) images obtained in one of two SCID mice bearing a subcutaneous BT474M1 xenograft after intravenous administration of [^{18}F]RL-I-2Rs15d (5.4 μg) are shown in Fig. 5a. For comparison, images obtained after injection of [^{18}F]RL-I-R3B23 nonspecific control sdAb in the same mouse are also shown (Fig. 5b). The %ID/g and, in parentheses, SUV values for tumor after injection of [^{18}F]RL-I-2Rs15d were 11.1 ± 3.4 %ID/g (1.9 ± 0.7), 10.8 ± 4.5 %ID/g (1.9 ± 0.8), and 10.9 ± 4.0 %ID/g (1.9 ± 0.7) at 1, 2, and 3 h p.i., respectively. In comparison, the values for [^{18}F]RL-I-R3B23 were 0.6 ± 0.2 %ID/g (0.1 ± 0.0) and 0.4 ± 0.1 %ID/g (0.1 ± 0.0) at 1 and 2 h, respectively, demonstrating HER2-specific uptake of [^{18}F]RL-I-2Rs15d in BT474M1 tumors. Tumor uptake in the second mouse injected with the same batch of [^{18}F]RL-I-2Rs15d was only ~5 %ID/g; however, at necropsy, this xenograft was found to have a large necrotic

component. Tumor-to-muscle ratios for [^{18}F]RL-I-2Rs15d over the 1–3-h study period for these two mice were 10–58:1. As seen in the necropsy experiment, liver uptake was rather high. Another mouse was imaged on an earlier date after administration of [^{18}F]RL-I-2Rs15d (13 μg) and had a %ID/g (SUV) tumor uptake of 4.8 %ID/g (0.8), 13.9 %ID/g (2.4), and 15.5 %ID/g (2.7) at 1, 2, and 3 h, respectively. With this preparation, liver uptake was only 0.5–1.3 %ID/g, considerably lower than that observed with the other batch.

MIP images obtained from a mouse bearing the intracranial BT474M1Br-Fluc tumor 1 h after administration of [^{18}F]RL-I-5F7, [^{18}F]RL-I-2Rs15d, and [^{18}F]RL-I-R3B23 are shown in Fig. 6a. Clear delineation of tumor can be seen in mice injected with the HER2-reactive sdAbs 5F7 and 2Rs15d but not when the mouse was injected with irrelevant sdAb R3B23. Percent injected dose per gram (SUV in parentheses) values for tumor were 6.4 %ID/g (1.5), 6.4 %ID/g (1.5), and 1.2 %ID/g (0.2) for [^{18}F]RL-I-5F7, [^{18}F]RL-I-2Rs15d, and [^{18}F]RL-I-R3B23, respectively. The PET detection of the intracranial tumor using our anti-HER2 radiotracers correlated well with the anatomical location of the tumor in the mouse brain (Fig. 6b).

Discussion

The significance of assessing HER2 status either for stratification of breast cancer patients for HER2-targeted therapy or for determining the effectiveness of these therapies has been emphasized [34, 35]. PET imaging is a noninvasive method that is being actively investigated for accurate quantification of HER2 status. Among the various targeting vectors that are being pursued for this purpose, sdAbs are attractive due to their favorable properties for PET imaging including rapid tumor targeting and fast clearance from normal tissues. Earlier, we evaluated an anti-HER2 sdAb 5F7 labeled with F-18 using a novel residualizing label as a radiotracer for potential assessment of HER2 status [19]. Because of the rapid internalization of 5F7 after binding to HER2 [36], a labeling method that generates labeled species that are trapped within the cell after receptor-mediated internalization could help maximize F-18 signal in HER2-positive tumor cells. However, the fact that binding of the 5F7 sdAb to HER2 is blocked by trastuzumab complicates its use in the evaluation of the effectiveness of HER2-targeted therapy because tracer uptake could be hampered by circulating therapeutic antibody. Another anti-HER2 sdAb, 2Rs15d, which binds to an HER2 epitope distinct from those targeted by trastuzumab and pertuzumab, has been labeled with Ga-68 and evaluated in a phase I study in HER2-positive breast cancer patients [17]. Motivated by these promising results and the potential advantages that might be gained by utilizing a longer half-life radionuclide with lower energy positron emission [37], we embarked on the current study, to evaluate the potential usefulness of 2Rs15d labeled with F-18 using the residualizing label [^{18}F]RL-I [25].

In the internalization and cell processing assays, the total cellular retention and intracellular radioactivity levels in BT474M1 cells for [^{18}F]RL-I-2Rs15d and co-incubated [^{125}I]SGMIB-2Rs15d were similar at all time points. This indicates that, as seen with 5F7 sdAb [19], the ability of the RL-I prosthetic agent to retain radioactivity within tumor cells after receptor-mediated internalization was comparable to its conceptual parent SGMIB [26], which utilizes a guanidino substituent to achieve residualizing ability. Compared with

the results obtained with [^{18}F]RL-I-5F7 (~50 % internalized maintained for 4 h) [19], the percentage of initially bound [^{18}F]RL-I-2Rs15d that internalized in BT474M1 cells was lower (44 %) and decreased to 22 % by 4 h, indicating differences between the two anti-HER2 sdAb with regard to both initial degree of internalization and intracellular retention kinetics. With regard to the effect of radionuclide and labeling method on these parameters, we note that in a previous study with 5F7 (with a cys-tag) labeled using [^{125}I]SGMIB, intracellular retention in this cell line was maintained at about 60 % for up to 24 h as was the case with another residualizing radioiodination agent [36]. The 2Rs15d sdAb has been radiolabeled with several radionuclides including F-18 [18], Ga-68 [24], Tc-99m [23], and Lu-177 [38, 39]; however, these publications did not include internalization experiments for comparison to the current study.

Differences in cellular retention of the two anti-HER2 sdAbs most likely reflect the fact that they bind to different sites on the HER2 molecule. The sdAb 5F7 competes with trastuzumab, which binds to domain IV of HER2, which is closest to the cell membrane [40]. On the other hand, 2Rs15d does not compete with trastuzumab or another clinically utilized anti-HER2 therapeutic antibody pertuzumab, which binds to the central region of domain II of HER2 [41]. Our previous work with intact antibodies targeting different HER2 epitopes demonstrated considerable differences in internalization and intracellular trapping of radioactivity [42]. In addition to the location of the binding epitope, studies with intact antibodies have shown that other factors including affinity can also play a role in determining internalization behavior [43]. Because lysosomal degradation is proportional to the internalization rate [44], we posit that 5F7 may be internalizing faster than 2Rs15d and thus undergoing more rapid intracellular degradation than 2Rs15d. This in turn may result in higher residualization of radioactivity from 5F7 due to a greater trapping of its labeled catabolites. On the other hand, more non-degraded 2Rs15d may be recycling back to the cell surface. However, Ward and Kaplan [45] have concluded that recycling cannot account for the differences in internalization rate. Finally, a lower degree of internalization increases residence time on the cell membrane where dissociation from the receptor can occur.

Necropsy experiments indicated a high level of tumor uptake for [^{18}F]RL-I-2Rs15d in BT474M1 xenografts, which was comparable to that seen for co-injected [^{125}I]SGMIB-2Rs15d. However, unlike the results obtained with [^{125}I]SGMIB-2Rs15d or observed previously with [^{18}F]RL-I-5F7 [19], unexpectedly high liver, lung, and spleen activity levels were seen with [^{18}F]RL-I-2Rs15d. Consistent with this, microPET/CT imaging studies with [^{18}F]RL-I-2Rs15d also showed that while the BT474M1 xenografts could be clearly delineated, there was considerable hepatic uptake in addition to the high uptake seen in the kidneys and bladder that is typically observed with sdAb molecules. The presence of aggregates in the labeled sdAb could explain this behavior; however, SDS-PAGE did not indicate the presence of significant aggregation of [^{18}F]RL-I-2Rs15d in the preparations used for these animal studies. The liver is not known to express HER2 at high levels; moreover, this sdAb does not cross-react with mouse HER2. We note that hepatic uptake in mice bearing SKOV3 xenografts and receiving either [^{68}Ga]NOTA-2Rs15d or [^{18}F]SFB-2Rs15d [18, 24] was lower than that reported in the current study. However, we also note that [^{68}Ga]2Rs15d uptake in the liver, lungs, and spleen decreased with increasing mass of administered sdAb. For example, spleen uptake of Ga-68-labeled 2Rs15d decreased

by nearly a factor of 4 when the injected mass was increased from 0.1 to 10 μg. It is highly likely that the mass amount of 2Rs15d administered had a role in the difference seen in liver uptake of [^{18}F]RL-I-2Rs15d between the two imaging experiments in the current study. Although not to the same degree as observed with [^{18}F]RL-I-2Rs15d, the uptake of [^{18}F]RL-I-5F7 in the liver, spleen, and lungs was somewhat high [19]. Given that the uptake of co-administered [^{125}I]SGMIB-2Rs15d in the liver and other normal tissues was much lower in the necropsy experiment, it appears that the triazole moiety, and specifically the triazole moiety-2Rs15d combination, plays a role in causing higher uptake in these organs. Identification of catabolites in these organs may throw light on this, and we plan to investigate this in future experiments. Nonetheless, it is encouraging to note that the specificity of [^{18}F]RL-I-2Rs15d tumor uptake was demonstrated by the fact that tumor could not be visualized with [^{18}F]RL-I-R3B23, which exhibited a tumor uptake less than 10 % that of [^{18}F]RL-I-2Rs15d.

With the caveat that a different tumor model was used, the uptake of [^{18}F]RL-I-2Rs15d in HER2-expressing BT474M1 xenografts was 3–4-fold higher than that reported for 2Rs15d labeled using [^{18}F]SFB in the SK-OV-3 model [18]. Further, the tumor uptake of [^{18}F]SFB-2Rs15d decreased by 1.6-fold from 1 to 3 h. In contrast, the tumor uptake of [^{18}F]RL-I-2Rs15d remained constant (17.4 ± 2.8 %ID/g at 1 h, to 19.4 ± 2.6 % at 3 h), presumably reflecting the residualizing nature of the [^{18}F]RL-I prosthetic agent. As seen with [^{18}F]RL-I-5F7 [19], defluorination was minimal for [^{18}F]RL-I-2Rs15d with bone uptake values of 1 %ID/g or less, which may be due in part to defluorination. Tumor-to-blood and tumor-to-muscle ratios were high as seen for [^{18}F]RL-I-5F7 [19] and considerably higher than those reported for [^{18}F]SFB-2Rs15d [18]. However, tumor-to-liver and tumor-to-spleen uptake ratios for [^{18}F]RL-I-2Rs15d were lower, which might interfere with the detection of liver metastases that frequently occur in breast cancer patients.

HER2-positive breast cancers are known to metastasize to the brain, and this has become an increasingly significant problem in part because trastuzumab can frequently control systemic disease but is ineffective against brain metastases because of its inability to cross the blood-brain barrier [46, 47]. The ability to image HER2-positive brain metastases in breast cancer patients could be an important tool in the management of these patients. Despite the inability of trastuzumab to cross the intact blood-brain barrier, Dijkers et al. [48] have demonstrated that brain metastases in breast cancer patients could be visualized by PET with Zr-89-labeled trastuzumab, presumably reflecting disruption of the blood-brain barrier in these lesions. However, given the about 10-fold lower molecular weight of sdAbs compared with intact mAbs, sdAbs may be a better vehicle for this purpose because of potentially lower nonspecific uptake in tumors due to the EPR effect. To evaluate this possibility, F-18-labeled sdAbs were injected intravenously into mice bearing intracranial HER2-expressing BT474M1BrM3 tumors. Interestingly, while both 5F7 and 2Rs15d were able to target the intracranial tumor, this was not the case with nonspecific control sdAb. Although preliminary, our results indicate that specific targeting of HER2-expressing intracranial tumors after intravenous injection is possible. Further investigation of the influence of factors such as blood-tumor barrier permeability, tumor size, and heterogeneity of HER2 expression on specific uptake of radiolabeled sdAbs in HER2-positive brain metastases is warranted.

Conclusion

The anti-HER2 sdAb 2Rs15d was labeled with F-18 using the residualizing labeling agent [^{18}F]RL-I in reasonable yields with preservation of immunoreactivity and affinity for HER2. *In vitro* studies demonstrated significant internalization of [^{18}F]RL-I-2Rs15d by HER2-expressing BT474M1 cells, although retention of radioactivity in the intracellular compartment was less than that observed previously with [^{18}F]RL-I-5F7. Tumor retention of F-18 activity in both subcutaneous and intracranial BT474M1 xenografts was greater than 15 and 6 %ID/g, respectively, and higher than that observed in the same animals for non-HER2-targeted control sdAb. While these results are encouraging, further optimization is required to decrease liver accumulation, which could interfere with detection of hepatic metastases.

Acknowledgments

This work was supported in part by National Institutes of Health grants CA188177 and CA42324 and, for small-animal PET imaging, by S10RR31792. Excellent technical assistance of Elzbieta Krol (*in vitro* studies) and Xiao-guang Zhao (*in vivo* studies) is greatly appreciated. We also thank Thomas Hawk, Yulin Zhao, and Simone Degan for their excellent support with microPET/CT imaging studies.

References

1. Schettini F, Buono G, Cardalesi C, et al. Hormone receptor/human epidermal growth factor receptor 2-positive breast cancer: where we are now and where we are going. Cancer Treat Rev. 2016; 46:20–26. [PubMed: 27057657]
2. Santa-Maria CA, Nye L, Mutonga MB, et al. Management of metastatic HER2-positive breast cancer: where are we and where do we go from here? Oncology (Williston Park). 2016; 30:148–155. [PubMed: 26892151]
3. Recondo G Jr, de la Vega M, Galanternik F, et al. Novel approaches to target HER2-positive breast cancer: trastuzumab emtansine. Cancer Manag Res. 2016; 8:57–65. [PubMed: 27274311]
4. Maximiano S, Magalhaes P, Guerreiro MP, Morgado M. Trastuzumab in the treatment of breast cancer. BioDrugs. 2016; 30:75–86. [PubMed: 26892619]
5. Gebhart G, Flamen P, De Vries EG, et al. Imaging diagnostic and therapeutic targets: human epidermal growth factor receptor 2. J Nucl Med. 2016; 57(Suppl 1):81S–88S. [PubMed: 26834107]
6. Nitta H, Kelly BD, Allred C, et al. The assessment of HER2 status in breast cancer: the past, the present, and the future. Pathol Int. 2016; 66:313–324. [PubMed: 27061008]
7. Karagoz Ozen DS, Ozturk MA, Aydin O, et al. Receptor expression discrepancy between primary and metastatic breast cancer lesions. Oncol Res Treat. 2014; 37:622–626. [PubMed: 25427579]
8. Rack B, Zombirt E, Trapp E, et al. Comparison of HER2 expression in primary tumor and disseminated tumor cells in the bone marrow of breast cancer patients. Oncology. 2016; 90:232–238. [PubMed: 26937631]
9. Kramer-Marek G, Oyen WJ. Targeting the human epidermal growth factor receptors: imaging biomarkers from bench to bedside. J Nucl Med. 2016; 57:996–1001. [PubMed: 27173163]
10. Sorensen J, Velikyan I, Sandberg D, et al. Measuring HER2-receptor expression in metastatic breast cancer using [^{68}Ga]ABY-025 affibody PET/CT. Theranostics. 2016; 6:262–271. [PubMed: 26877784]
11. Mendler CT, Gehring T, Wester HJ, et al. ^{89}Zr-labeled versus ^{124}I-labeled αHER2 Fab with optimized plasma half-life for high-contrast tumor imaging in vivo. J Nucl Med. 2015; 56:1112–1118. [PubMed: 25999431]
12. Ma T, Sun X, Cui L, et al. Molecular imaging reveals trastuzumab-induced epidermal growth factor receptor downregulation in vivo. J Nucl Med. 2014; 55:1002–1007. [PubMed: 24732154]

13. Olafsen T, Sirk SJ, Olma S, et al. ImmunoPET using engineered antibody fragments: fluorine-18 labeled diabodies for same-day imaging. Tumour Biol. 2012; 33:669–677. [PubMed: 22392499]
14. Olafsen T, Kenanova VE, Sundaresan G, et al. Optimizing radiolabeled engineered anti-p185HER2 antibody fragments for in vivo imaging. Cancer Res. 2005; 65:5907–5916. [PubMed: 15994969]
15. Kijanka M, Dorresteijn B, Oliveira S, van Bergen en Henegouwen PM. Nanobody-based cancer therapy of solid tumors. Nanomedicine. 2015; 10:161–174. [PubMed: 25597775]
16. De Meyer T, Muyldermans S, Depicker A. Nanobody-based products as research and diagnostic tools. Trends Biotechnol. 2014; 32:263–270. [PubMed: 24698358]
17. Keyaerts M, Xavier C, Heemskerk J, et al. Phase I study of ^{68}Ga-HER2-nanobody for PET/CT assessment of HER2 expression in breast carcinoma. J Nucl Med. 2016; 57:27–33. [PubMed: 26449837]
18. Xavier C, Blykers A, Vaneycken I, et al. ^{18}F-nanobody for PET imaging of HER2 overexpressing tumors. Nucl Med Biol. 2016; 43:247–252. [PubMed: 27067045]
19. Vaidyanathan G, McDougald D, Choi J, et al. Preclinical evaluation of ^{18}F-labeled anti-HER2 nanobody conjugates for imaging HER2 receptor expression by immuno-PET. J Nucl Med. 2016; 57:967–973. [PubMed: 26912425]
20. Revets, HMBC., Hoogenboom, HM. Amino acid sequences directed against HER2 and polypeptides comprising the same for the treatment of cancers and/or tumors. US Patent. 2011/0059090 Al. 2011.
21. Rockberg J, Schwenk JM, Uhlen M. Discovery of epitopes for targeting the human epidermal growth factor receptor 2 (HER2) with antibodies. Mol Oncol. 2009; 3:238–247. [PubMed: 19393584]
22. Kramer-Marek G, Gijsen M, Kiesewetter DO, et al. Potential of PET to predict the response to trastuzumab treatment in an ErbB2-positive human xenograft tumor model. J Nucl Med. 2012; 53:629–637. [PubMed: 22410461]
23. Vaneycken I, Devoogdt N, Van Gassen N, et al. Preclinical screening of anti-HER2 nanobodies for molecular imaging of breast cancer. FASEB J. 2011; 25:2433–2446. [PubMed: 21478264]
24. Xavier C, Vaneycken I, D'Huyvetter M, et al. Synthesis, preclinical validation, dosimetry, and toxicity of ^{68}Ga-NOTA-anti-HER2 nanobodies for iPET imaging of HER2 receptor expression in cancer. J Nucl Med. 2013; 54:776–784. [PubMed: 23487015]
25. Vaidyanathan G, McDougald D, Choi J, et al. *N*-Succinimidyl 3-((4-(4-[^{18}F]fluorobutyl)-1H-1,2,3-triazol-1-yl)methyl)-5-(guanidinomethyl)ben zoate ([^{18}F]SFBTMGMB): a residualizing label for ^{18}F-labeling of internalizing biomolecules. Org Biomol Chem. 2016; 14:1261–1271. [PubMed: 26645790]
26. Vaidyanathan G, Zalutsky MR. Synthesis of *N*-succinimidyl 4-guanidinomethyl-3-[*I]iodobenzoate: a radio-iodination agent for labeling internalizing proteins and peptides. Nat Protoc. 2007; 2:282–286. [PubMed: 17406587]
27. Pruszynski M, Koumarianou E, Vaidyanathan G, et al. Targeting breast carcinoma with radioiodinated anti-HER2 nanobody. Nucl Med Biol. 2013; 40:52–59. [PubMed: 23159171]
28. Gray MA, Tao RN, DePorter SM, et al. A nanobody activation immunotherapeutic that selectively destroys HER2-positive breast cancer cells. Chembiochem. 2016; 17:155–158. [PubMed: 26556305]
29. Lemaire M, D'Huyvetter M, Lahoutte T, et al. Imaging and radioimmunotherapy of multiple myeloma with anti-idiotypic nanobodies. Leukemia. 2014; 28:444–447. [PubMed: 24166214]
30. Yu Z, Xia W, Wang HY, et al. Antitumor activity of an Ets protein, PEA3, in breast cancer cell lines MDA-MB-361DYT2 and BT474M1. Mol Carcinog. 2006; 45:667–675. [PubMed: 16652376]
31. Choi J, Vaidyanathan G, Koumarianou E, et al. *N*-Succinimidyl guanidinomethyl iodobenzoate protein radiohalogenation agents: influence of isomeric substitution on radiolabeling and target cell residualization. Nucl Med Biol. 2014; 41:802–812. [PubMed: 25156548]
32. Lindmo T, Boven E, Cuttitta F, et al. Determination of the immunoreactive fraction of radiolabeled monoclonal antibodies by linear extrapolation to binding at infinite antigen excess. J Immunol Meth. 1984; 72:77–89.

33. Kanojia D, Balyasnikova IV, Morshed RA, et al. Neural stem cells secreting anti-HER2 antibody improve survival in a preclinical model of HER2 overexpressing breast cancer brain metastases. Stem Cells. 2015; 33:2985–2994. [PubMed: 26260958]
34. Velikyan I, Wennborg A, Feldwisch J, et al. Good manufacturing practice production of [^{68}Ga]Ga-ABY-025 for HER2 specific breast cancer imaging. Am J Nucl Med Mol Imaging. 2016; 6:135–153. [PubMed: 27186441]
35. Trousil S, Hoppmann S, Nguyen QD, et al. Positron emission tomography imaging with ^{18}F-labeled ZHER2:2891 affibody for detection of HER2 expression and pharmacodynamic response to HER2-modulating therapies. Clin Cancer Res. 2014; 20:1632–1643. [PubMed: 24493830]
36. Pruszynski M, Koumarianou E, Vaidyanathan G, et al. Improved tumor targeting of anti-HER2 nanobody through *N*-succinimidyl 4-guanidinomethyl-3-iodobenzoate radiolabeling. J Nucl Med. 2014; 55:650–656. [PubMed: 24578241]
37. Sanchez-Crespo A. Comparison of gallium-68 and fluorine-18 imaging characteristics in positron emission tomography. Appl Radiat Isot. 2013; 76:55–62. [PubMed: 23063597]
38. D'Huyvetter M, Aerts A, Xavier C, et al. Development of ^{177}Lu-nanobodies for radioimmunotherapy of HER2-positive breast cancer: evaluation of different bifunctional chelators. Contrast Media Mol Imaging. 2012; 7:254–264. [PubMed: 22434639]
39. D'Huyvetter M, Vincke C, Xavier C, et al. Targeted radionuclide therapy with a ^{177}Lu-labeled anti-HER2 nanobody. Theranostics. 2014; 4:708–720. [PubMed: 24883121]
40. Banappagari S, McCall A, Fontenot K, et al. Design, synthesis and characterization of peptidomimetic conjugate of BODIPY targeting HER2 protein extracellular domain. Eur J Med Chem. 2013; 65:60–69. [PubMed: 23688700]
41. Fuentes G, Scaltriti M, Baselga J, Verma CS. Synergy between trastuzumab and pertuzumab for human epidermal growth factor 2 (Her2) from colocalization: an in silico based mechanism. Breast Cancer Res. 2011; 13:R54. [PubMed: 21600050]
42. Xu FJ, Yu YH, Bae DS, et al. Radioiodinated antibody targeting of the HER-2/neu oncoprotein. Nucl Med Biol. 1997; 24:451–459. [PubMed: 9290082]
43. Langmuir VK, Mendonca HL, Woo DV. Comparisons between two monoclonal antibodies that bind to the same antigen but have differing affinities: uptake kinetics and ^{125}I-antibody therapy efficacy in multicell spheroids. Cancer Res. 1992; 52:4728–4734. [PubMed: 1511438]
44. Wargalla UC, Reisfeld RA. Rate of internalization of an immunotoxin correlates with cytotoxic activity against human tumor cells. Proc Natl Acad Sci U S A. 1989; 86:5146–5150. [PubMed: 2544891]
45. Ward DM, Kaplan J. The rate of internalization of different receptor-ligand complexes in alveolar macrophages is receptor-specific. Biochem J. 1990; 270:369–374. [PubMed: 1698058]
46. Stemmler HJ, Schmitt M, Harbeck N, et al. Application of intrathecal trastuzumab (Herceptin trademark) for treatment of meningeal carcinomatosis in HER2-overexpressing metastatic breast cancer. Oncol Rep. 2006; 15:1373–1377. [PubMed: 16596213]
47. Stemmler HJ, Schmitt M, Willems A, et al. Ratio of trastuzumab levels in serum and cerebrospinal fluid is altered in HER2-positive breast cancer patients with brain metastases and impairment of blood-brain barrier. Anti-Cancer Drugs. 2007; 18:23–28. [PubMed: 17159499]
48. Dijkers EC, Oude Munnink TH, Kosterink JG, et al. Biodistribution of ^{89}Zr-trastuzumab and PET imaging of HER2-positive lesions in patients with metastatic breast cancer. Clin Pharmacol Ther. 2010; 87:586–592. [PubMed: 20357763]

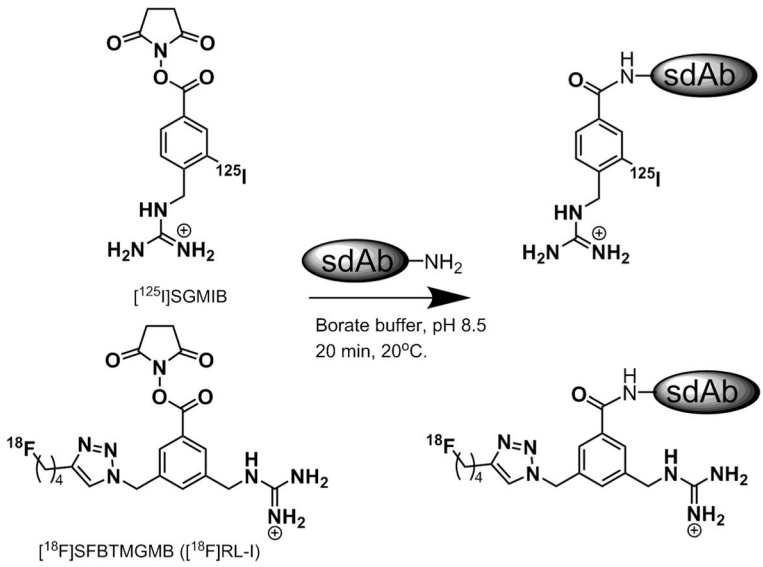

Fig. 1.
Structures of residualizing prosthetic agents [*I]SGMIB and [^{18}F]RL-I.

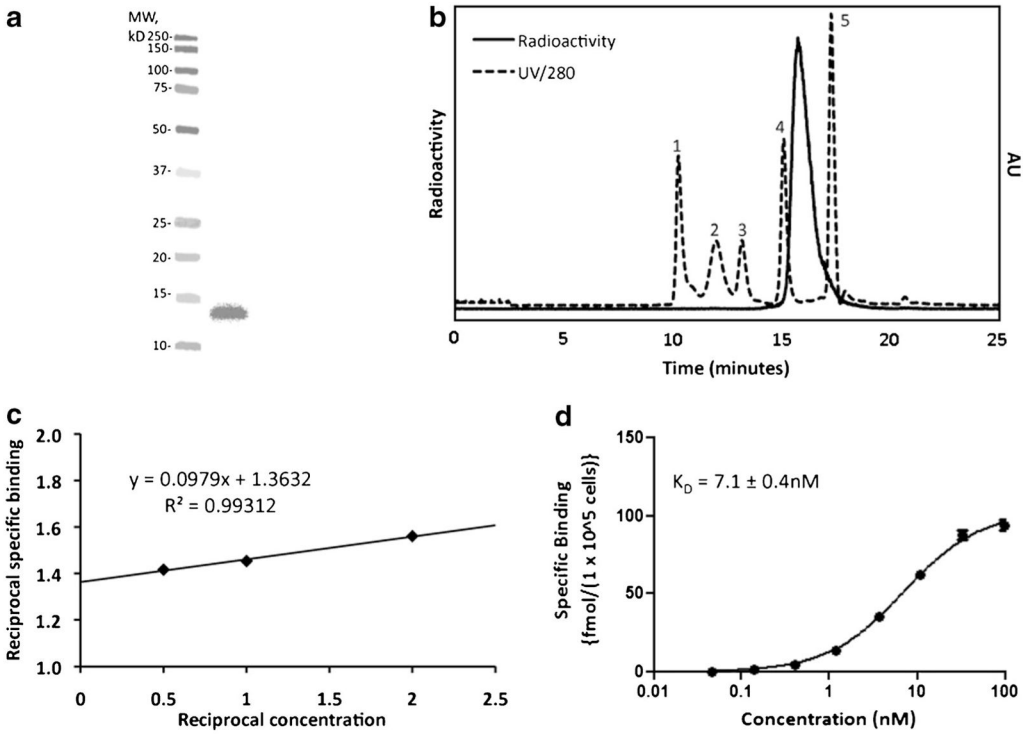

Fig. 2.

Quality control data for a typical batch of [^{18}F]RL-I-2Rs15d. **a** SDS-PAGE/phosphor imaging showing only one band corresponding to the molecular weight of sdAb—*left lane* molecular weight markers and *right lane* [^{18}F]RL-I-2Rs15d. **b** Size-exclusion HPLC profile of labeled 2Rs15d (*solid line*). As a reference, the UV HPLC profile of standards of different molecular weight is also shown (*dashed line*)—*1* thyroglobulin (670 kDa), *2* γ-globulin (158 kDa), *3* ovalbumin (44 kDa), *4* myoglobin (17 kDa), *5* vitamin B_{12} (1.4 kDa). **c** Immunoreactivity assay data. **d** Saturation binding assay data obtained using BT474M1 cells.

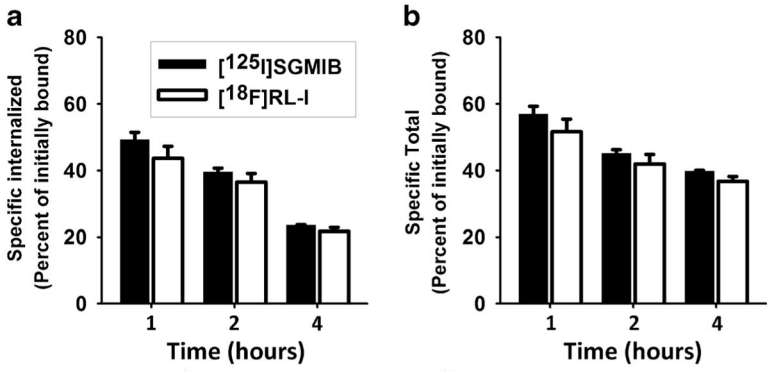

Fig. 3.

Paired-label internalization of [^{125}I]SGMIB-2Rs15d and [^{18}F]RL-I-2Rs15d. BT474M1 cells were incubated with [^{125}I]SGMIB-2Rs15d (*black*) and [^{18}F]RL-I-2Rs15d (*white*) at 4 °C for an hour, unbound radioactivity was removed, and after adding fresh medium, cells were brought to 37 °C and processed at 1, 2, and 4 h as described in the text. Data shown are percent of initially cell-bound radioactivity **a** that was internalized and **b** that was cell-associated (internalized + surface-bound).

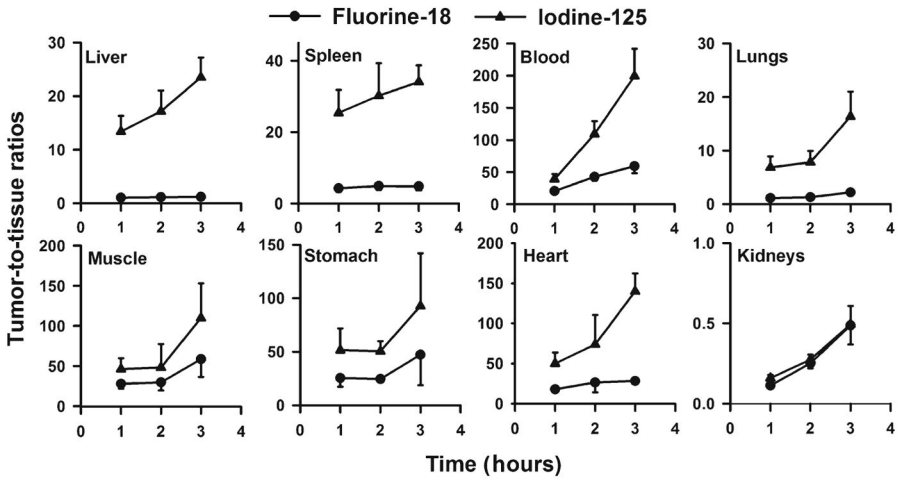

Fig. 4.

Tumor-to-tissue ratios calculated for F-18 (*circle*) and I-125 (*triangle*) from the data (Table 1) obtained from the paired-label biodistribution of [^{18}F]RL-I-2Rs15d and [^{125}I]SGMIB-2Rs15d in SCID mice bearing BT474M1 xenografts.

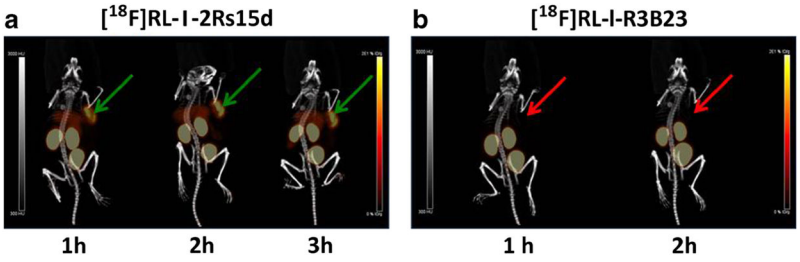

Fig. 5.

MicroPET/CT images obtained at **a** 1, 2, and 3 h p.i. of [^{18}F]RL-I-2Rs15d and **b** 1 and 2 h after injection of [^{18}F]RL-I-R3B23 in SCID mice bearing BT474M1 xenografts. The green (2Rs15d) and red (R3B23) arrows point to the position of tumor in the mice

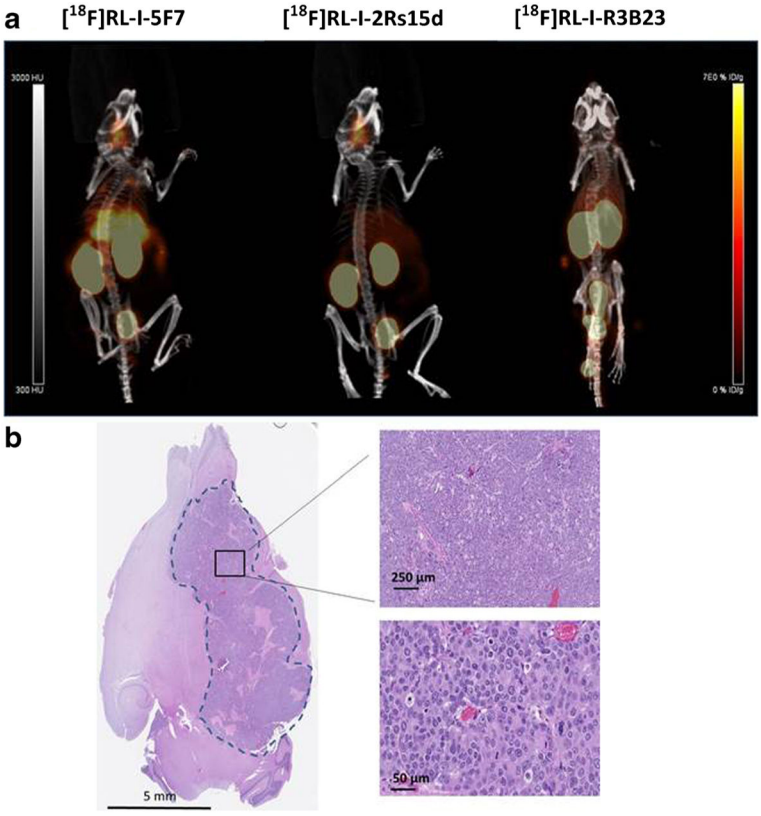

Fig. 6.

a MicroPET/CT images obtained 1 h after i.v. injection of (*left* to *right*) [^{18}F]RL-I-5F7, [^{18}F]RL-I-2Rs15d, and [^{18}F]RL-I-R3B23 in mice bearing BT474M1BrM3-Fluc intracranial xenografts. **b** After microPET/CT imaging, mouse brains were collected and preserved as described in “Materials and Methods.” Four-micrometer brain tissue sections were stained with H&E dye to confirm the tumor distribution in the mouse brain.

Table 1

Paired-label biodistribution of 2Rs15d labeled using [^{125}I]SGMIB and [^{18}F]RL-I

Tissue	Percent injected dose per gram[a]					
	1 h		2 h		3 h	
	I-125	F-18	I-125	F-18	I-125	F-18
Liver	1.56 ± 0.15	16.75 ± 2.13	1.18 ± 0.21	14.13 ± 1.47	1.01 ± 0.09	16.58 ± 1.97
Spleen	0.84 ± 0.16	4.22 ± 0.97	0.68 ± 0.13	3.29 ± 0.47	0.70 ± 0.13	4.17 ± 0.70
Lungs	3.17 ± 0.75	15.65 ± 2.66	2.62 ± 0.63	12.43 ± 1.88	1.53 ± 0.44	9.15 ± 2.11
Heart	0.43 ± 0.12	0.98 ± 0.20	0.55 ± 0.72	0.81 ± 0.62	0.17 ± 0.03	0.69 ± 0.12
Kidneys	129.56 ± 7.05	154.45 ± 18.55	71.88 ± 10.34	63.37 ± 10.46	49.13 ± 9.38	41.61 ± 9.98
Stomach	0.46 ± 0.19	0.74 ± 0.27	0.30 ± 0.06	0.65 ± 0.10	0.34 ± 0.24	0.83 ± 1.03[c]
Small intestine	0.49 ± 0.15	2.49 ± 0.37	0.40 ± 0.06	2.00 ± 0.40	0.33 ± 0.07	2.00 ± 0.21
Large intestine	0.32 ± 0.06	0.79 ± 0.12	0.52 ± 0.13	1.68 ± 0.35	0.64 ± 0.21	2.88 ± 0.47
Thyroid[b]	0.01 ± 0.03	0.06 ± 0.02	0.00 ± 0.00	0.00 ± 0.00[c]	0.00 ± 0.00	0.01 ± 0.12[c]
Muscle	0.47 ± 0.14	0.63 ± 0.09	0.54 ± 0.31	0.60 ± 0.27[c]	0.25 ± 0.13	0.36 ± 0.11
Blood	0.55 ± 0.13	0.86 ± 0.14	0.18 ± 0.04	0.38 ± 0.09	0.12 ± 0.04	0.34 ± 0.08
Bone	0.59 ± 0.24	1.01 ± 0.26	0.60 ± 0.42	0.97 ± 0.33	0.17 ± 0.07	0.69 ± 0.16
Brain	0.04 ± 0.01	0.06 ± 0.01	0.05 ± 0.03	0.06 ± 0.03	0.02 ± 0.01	0.04 ± 0.01
Tumor	20.65 ± 2.78	17.41 ± 2.81	19.64 ± 3.01	15.81 ± 2.53	23.51 ± 2.74	19.43 ± 2.59

[a] Mean ± SD (n = 5)

[b] Percent injected dose per organ

[c] Difference in uptake between the two agents statistically *not* significant